Supporting Information for "Ultra-low velocity zone beneath the Atlantic near St. Helena"

Felix Davison [1], Carl Martin [1,2], Rita Parai [3], Sanne Cottaar [1]

[1]Department of Earth Sciences, University of Cambridge

[2]Faculty of Geosciences, Utrecht University

[3]Department of Earth, Environmental, and Planetary Sciences, Washington University in St. Louis

Contents of this file

Corresponding author: F. Davison, Department of Earth Sciences, University of Cambridge (fpd21@cam.ac.uk)

March 8, 2024, 2:18pm

1. Events considered

Our data search considered 27 promising events around the Atlantic Ocean as listed in Table S1. A large number of these events show the presence of postcursors. For some events the Sdiff coverage has no or few paths in the area where we eventually find the ULVZ. Other events are poor in quality. The four events modelled in detail in the main paper are chosen for their quality and diversity in azimuthal sampling.

Modelling was also carried out on two further events for which we show the results for the preferred model here. The 2018/12/11 South Sandwich Islands earthquake (event S1, Figure S2) samples across Europe in a geometry similar to event C. Synthetics with our preferred ULVZ show postcursors that are comparable to what is seen in the real data. We also provide an example of less optimal event, where postcursors should be expected, but are not clearly seen (event S2, Figure S3). This event occurred in the Drake Passage and samples the ULVZ from a slightly different angle. The synthetics predict a fairly strong postcursor should be visible for stations in and around Greece and Turkey. The postcursor is not clear in the data, although the data are relatively noisy. There are potentially some unmodelled asymmetries in the ULVZ morphology that could further explain a reduction in the postcursor amplitude here.

2. Data Selection and Rejection

The data selection algorithm employed was designed to perform the maximum degree of quality control possible with the minimum number of constraints. Initially, the two rules applied were that the minimum correlation between a given trace and the average waveform across all stations had to exceed 0.2; and that the correlation to the average waveform from stations within one degree of azimuth had to exceed the correlation to the average waveform across all stations. Figure S4 shows the results of this selection for event A.

The main arrival in the rejected waveforms, at around 30 seconds after the predicted Sdiff arrival, is still relatively clear; however, the trend in move-out, with the greatest delay in the main arrival being at around 295° azimuth, is only visible in the accepted waveforms.

This algorithm is flawed in that in cases where the local average is very similar to the global average, many waveforms can be erroneously rejected, as shown in Figure S5 for event C. Notably, every waveform in the 17° bin has been rejected. This issue does not affect the observation of postcursor trends that we focus on here. Regardless, one additional rule - accepting any waveform for which *either* the local or global correlation coefficient exceeded 0.8, regardless of which coefficient was greater - can largely correct this issue. With this change, the results for event C are a much closer visual match for what would be manually selected by a seismologist. The adjusted algorithm was used for the data selection in the main paper.

3. Trade-offs and Uncertainties in our Model

3.1. Model ULVZ Position

We varied our model ULVZ position by 4° in latitude and longitude in four different directions (Figure S6). On the core-mantle boundary these shifts are slightly further than the ULVZ radius of 300 km. The synthetic waveforms for each of the shifts for event A is shown in Figure S7. Event A is sensitive to the NE-SW position of the ULVZ, and the waveforms show that models shifted in these directions shift where the postcursors are present as a function of azimuth. The waveforms also show that models along a NW-SE axis produce broadly equivalent results for event A to our preferred model. Results for Event D are shown in Figure S8, and this event provides a strong North-South constraint on the position of the ULVZ.

3.2. Height, Radius and Velocity Reduction

We tested models with varying heights, radii and velocity reductions. Results for some of these models are shown for event A (Figure S9) and C (Figure S10). The first tests show a thinner (10 km) and thicker (30 km) model. Thickness of the ULVZ affects both the amplitude and the delay time of the postcursor. Especially for the thinner model, the postcursor is clearly too weak. Additionally, we show results for a velocity reduction of 20% instead of 30%. Here we observe the postcursors starting to disappear, particularly for event C. The last test shows that a model with a wider radius of 450 km shows a stronger and more delayed postcursor. These tests show that it cannot be excluded that there are wider/thicker, but less reduced, models that would fit our data equally well.

4. Frequency Dependence

Haskell (1960) observes that the dominant period seen in waves trapped in finite sedimentary basins relate to the thickness of and the velocity within the basin. Here we use this relationship for a heuristic bound on the height of the ULVZ, as done in Cottaar and Romanowicz (2012). We take a shear velocity on the core-mantle boundary of around 5 km/s (PREM, Dziewonski & Anderson, 1981, reduced by 30% as per our preferred model). From this, Haskell's rule of thumb relates the dominant period band T to the ULVZ's height h via the shear velocity β:

$$T = 4h/\beta \tag{1}$$

Given our β value of 5 km/s, this tells us that the ULVZ's height will be $\frac{5}{4} * T$. Figures S11 to S14 show the real data for events A to D filtered to a range of narrow (5 s wide) period bands. The postcursors arguably appear strongest in the 10-15 s or 15-20 s period band, implying a height close to our preferred modelled value of 20 km. However, there is some variation, with the postcursor appearing strong at longer period for event C and a clear postcursor in the 5-10 s band for event D. For the 5-10 s period band, the signal-to-noise ratio is generally poor. The observed variation is likely due to the actual morphological variations of the ULVZ that are not captured by our simplified cylindrical model with a constant height of 20 km.

References

Cottaar, S., & Romanowicz, B. (2012). An unsually large ULVZ at the base of the mantle near Hawaii. *Earth and Planetary Science Letters*, *355*, 213–222. doi: https://doi.org/10.1016/j.epsl.2012.09.005

Dziewonski, A. M., & Anderson, D. L. (1981). Preliminary reference Earth model. *Physics of the earth and planetary interiors*, *25*(4), 297–356. doi: https://doi.org/10.1016/0031-9201(81)90046-7

Ekström, G., Nettles, M., & Dziewoński, A. (2012). The global CMT project 2004–2010: Centroid-moment tensors for 13,017 earthquakes. *Physics of the Earth and Planetary Interiors*, *200-201*, 1-9. doi: https://doi.org/10.1016/j.pepi.2012.04.002

French, S., & Romanowicz, B. A. (2014). Whole-mantle radially anisotropic shear velocity structure from spectral-element waveform tomography. *Geophysical Journal International*, *199*(3), 1303–1327. doi: https://doi.org/10.1093/gji/ggu334

Haskell, N. A. (1960). Crustal reflection of plane SH waves. *Journal of Geophysical Research (1896-1977)*, *65*(12), 4147-4150. doi: https://doi.org/10.1029/JZ065i012p04147

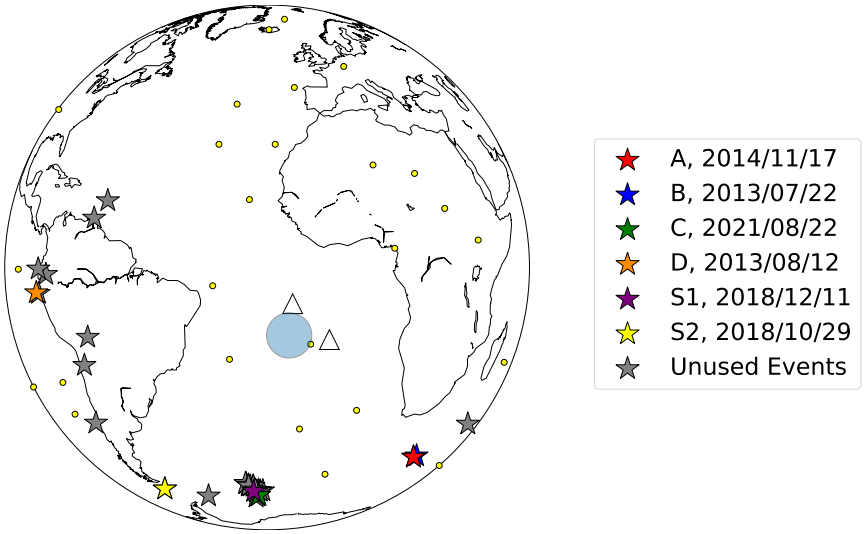

Figure S1. Map showing all events considered. Events A-D and S1-2 are coloured and labelled. Final ULVZ model is shown in blue circle. Major hotspots are shown as yellow circles and the volcanic islands of Ascension and St Helena are shown as triangles.

Date	Lon. [°E]	Lat. [°N]	Depth [km]	Location	Label
2000/09/28	-80.74	-0.32	15.0	NEAR COAST OF ECUADOR	
2008/06/30	-21.77	-58.33	26.01	SOUTH SANDWICH ISLANDS R	
2010/08/12	-77.51	-1.51	197.78	ECUADOR	
2010/12/08	-25.48	-56.49	18.3	SOUTH SANDWICH ISLANDS R	
2011/03/06	-26.68	-56.41	101.22	SOUTH SANDWICH ISLANDS R	
2011/06/20	-68.63	-21.89	131.37	CHILE-BOLIVIA BORDER REG	
2011/11/22	-65.18	-15.4	553.83	CENTRAL BOLIVIA	
2013/07/22	34.93	-45.89	20.71	PRINCE EDWARD ISLANDS RE	**Event B**
2013/07/26	-23.51	-58.12	17.39	SOUTH SANDWICH ISLANDS R	
2013/08/12	-82.13	-5.52	12.0	NEAR COAST OF NORTHERN P	**Event D**
2013/10/12	-62.15	10.86	78.39	NEAR COAST OF VENEZUELA	
2013/11/16	-47.0	-60.54	16.91	SCOTIA SEA	
2014/02/18	-58.89	14.76	13.91	NORTH ATLANTIC OCEAN	
2014/03/15	-81.1	-5.65	32.53	NEAR COAST OF NORTHERN P	
2014/06/29	-28.31	-55.34	20.99	SOUTH SANDWICH ISLANDS R	
2014/11/17	33.79	-46.27	17.65	PRINCE EDWARD ISLANDS RE	**Event A**
2015/02/16	-28.14	-55.5	14.24	SOUTH SANDWICH ISLANDS R	
2015/06/20	-74.1	-36.35	12.0	NEAR COAST OF CENTRAL CH	
2017/01/02	52.42	-36.63	15.15	SOUTHWEST INDIAN RIDGE	
2017/05/10	-25.51	-56.43	19.19	SOUTH SANDWICH ISLANDS R	
2018/10/29	-66.6	-57.55	20.66	DRAKE PASSAGE	**Event S2**
2018/12/11	-25.68	-58.58	147.08	SOUTH SANDWICH ISLANDS R	**Event S1**
2019/04/09	-24.6	-58.71	42.56	SOUTH SANDWICH ISLANDS R	
2019/05/27	-27.31	-56.39	122.25	SOUTH SANDWICH ISLANDS R	
2020/07/26	-25.01	-60.97	12.0	SOUTH SANDWICH ISLANDS R	
2021/07/17	-27.37	-56.04	109.63	SOUTH SANDWICH ISLANDS R	
2021/08/12	-24.34	-59.48	20.0	SOUTH SANDWICH ISLANDS R	
2021/08/16	-22.84	-58.45	15.47	SOUTH SANDWICH ISLANDS R	
2021/08/17	-24.79	-58.02	39.2	SOUTH SANDWICH ISLANDS R	
2021/08/22	-23.63	-60.32	12.0	SOUTH SANDWICH ISLANDS R	**Event C**
2021/08/22	-24.21	-60.56	12.0	SOUTH SANDWICH ISLANDS R	

Table S1. Earthquake source parameters. From the Global Centroid-Moment-Tensor project (Ekström et al., 2012).

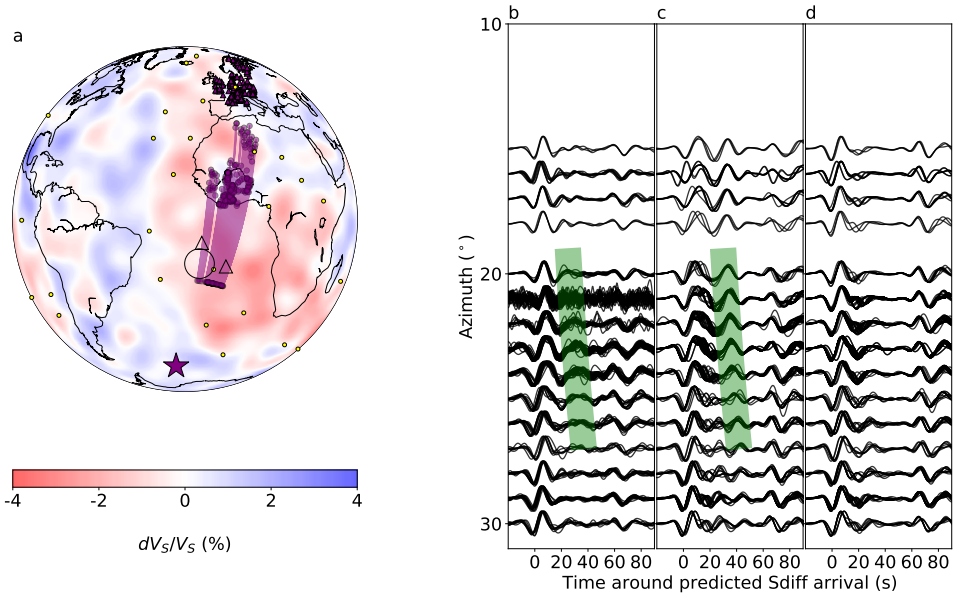

Figure S2. Coverage map, real and synthetic waveforms for Event S1 (2018/12/11). a. Map showing ray paths and proposed ULVZ location. Background velocity model is a depth slice through SEMUCB-WM1 (French & Romanowicz, 2014) at 2800 km depth. b. Observed data with interpreted postcursors highlighted in green. c. Synthetics including the proposed ULVZ model within SEMUCB-WM1. Same highlight is shown as in b. shifted by +5 seconds. d. Synthetics for SEMUCB-WM1.

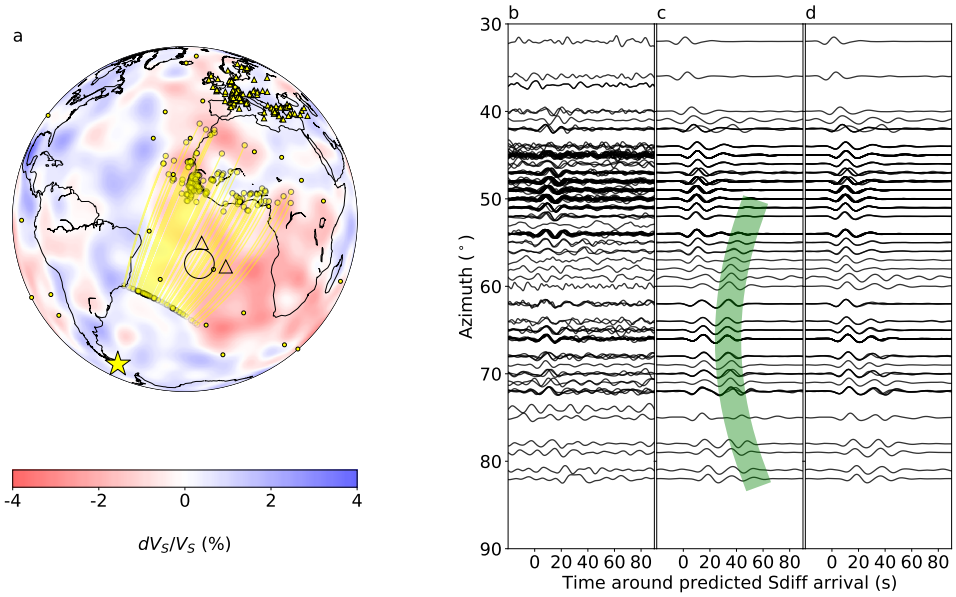

Figure S3. Coverage map, real and synthetic waveforms for event S2 (2018/10/29). a. Map showing ray paths and proposed ULVZ location. Background velocity model is a depth slice through SEMUCB-WM1 (French & Romanowicz, 2014) at 2800 km depth. b. Observed data with interpreted postcursors highlighted in green. c. Synthetics including the proposed ULVZ model within SEMUCB-WM1. Same highlight is shown as in b. shifted by -5 seconds. d. Synthetics for SEMUCB-WM1.

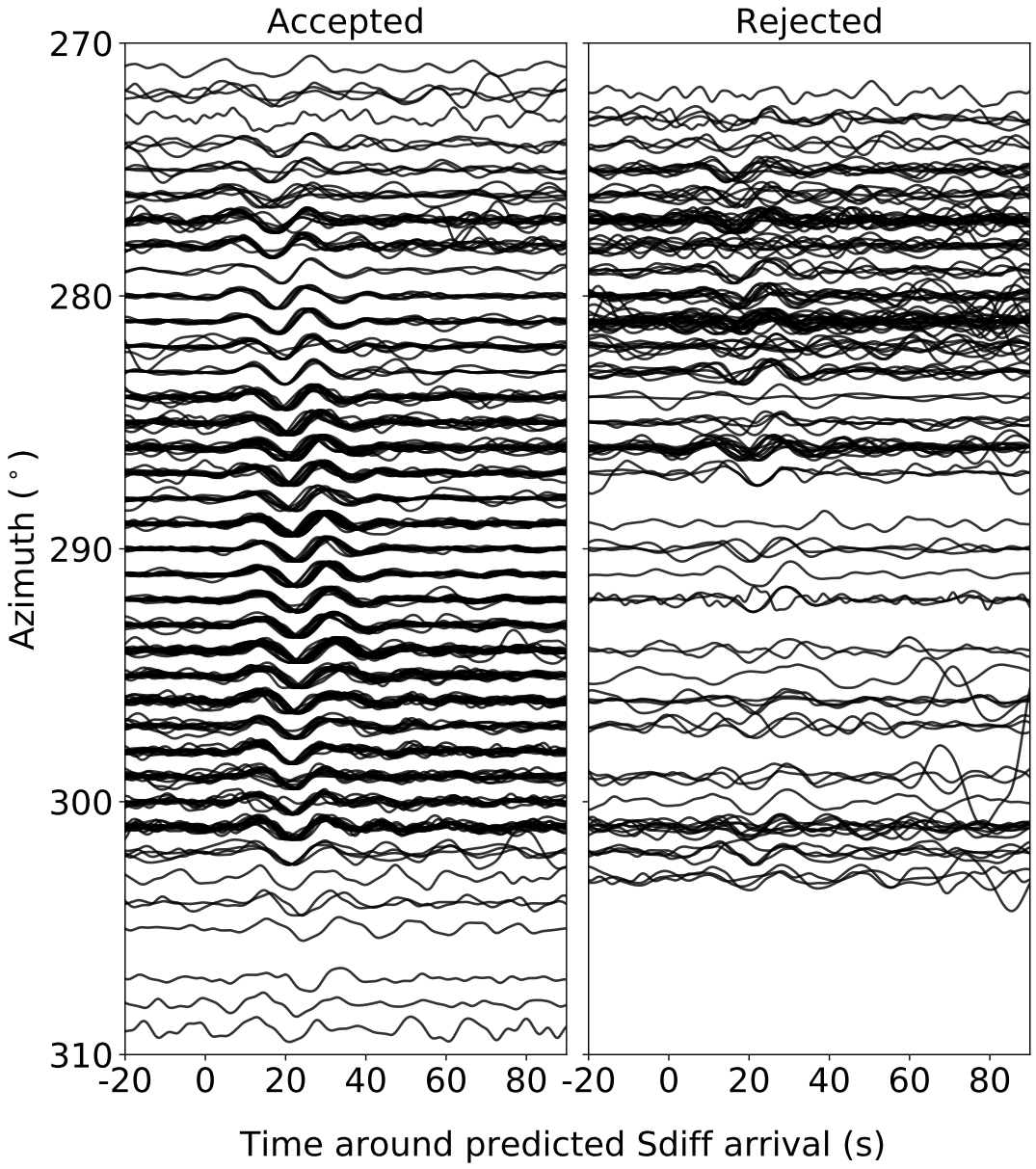

Figure S4. Accepted and rejected waveforms for event A using our automatic selection algorithm.

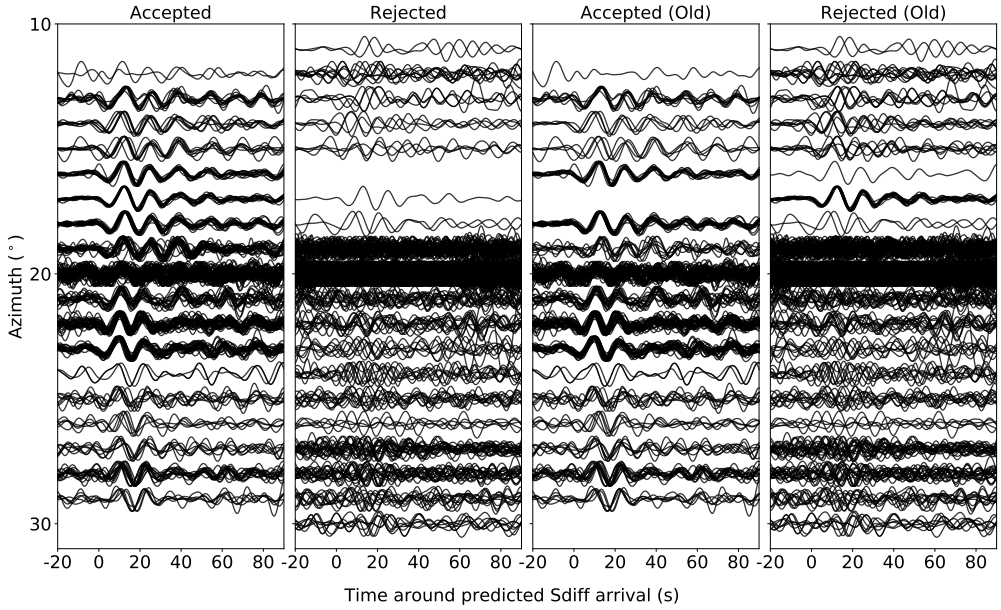

Figure S5. Accepted and rejected waveforms for event C using the refined rules of our automatic selection algorithm, with accepted and rejected waveforms by the old algorithm for comparison.

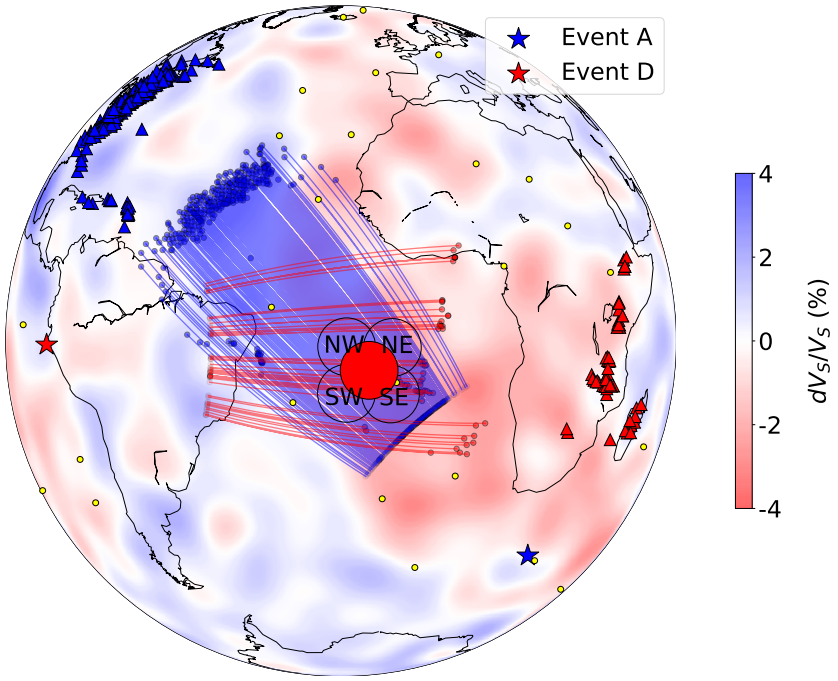

Figure S6. Map of different model ULVZ locations. Each model is stepped out 4° in both latitude and longitude from our preferred model. Waveforms for events A and D are overlaid. Background velocity model is a depth slice through SEMUCB-WM1 (French & Romanowicz, 2014) at 2800 km depth.

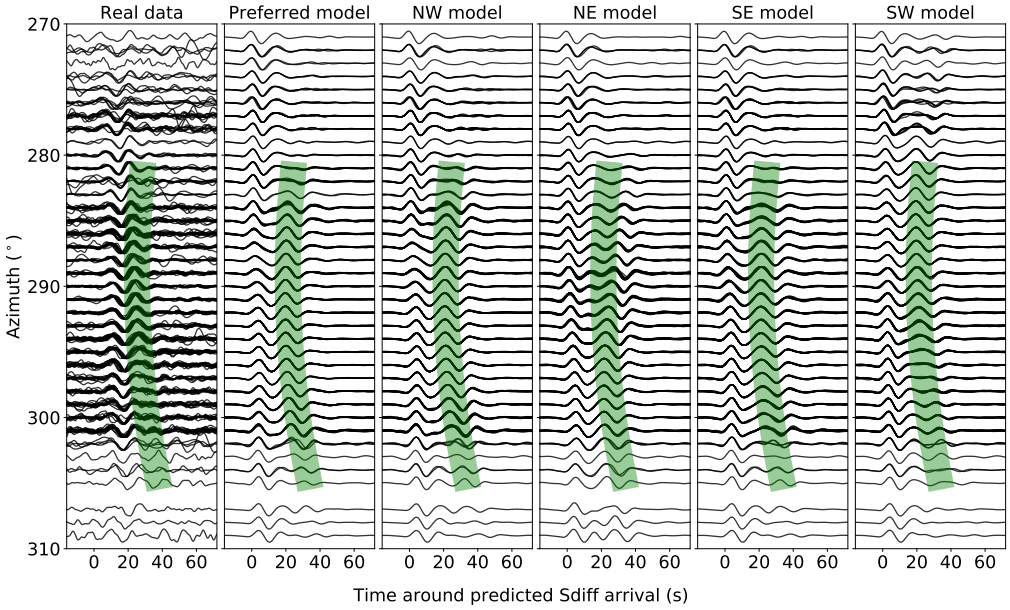

Figure S7. Waveform predictions for ULVZ models in different positions for event A. Each model is stepped out 4° in both latitude and longitude from our preferred model.

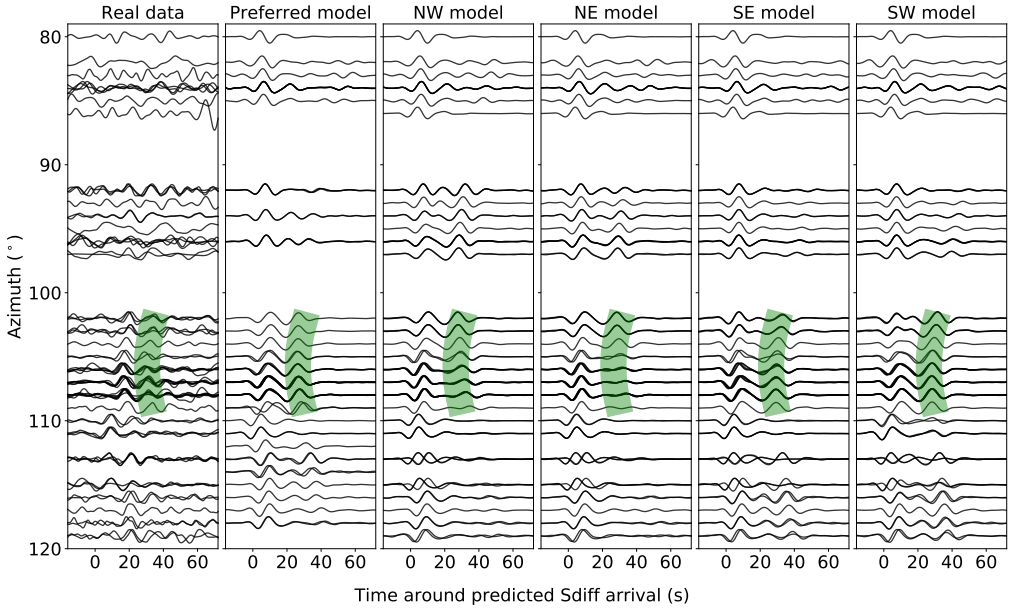

Figure S8. Waveform predictions for ULVZ models in different positions for event D. Each model is stepped out 4° in both latitude and longitude from our preferred model.

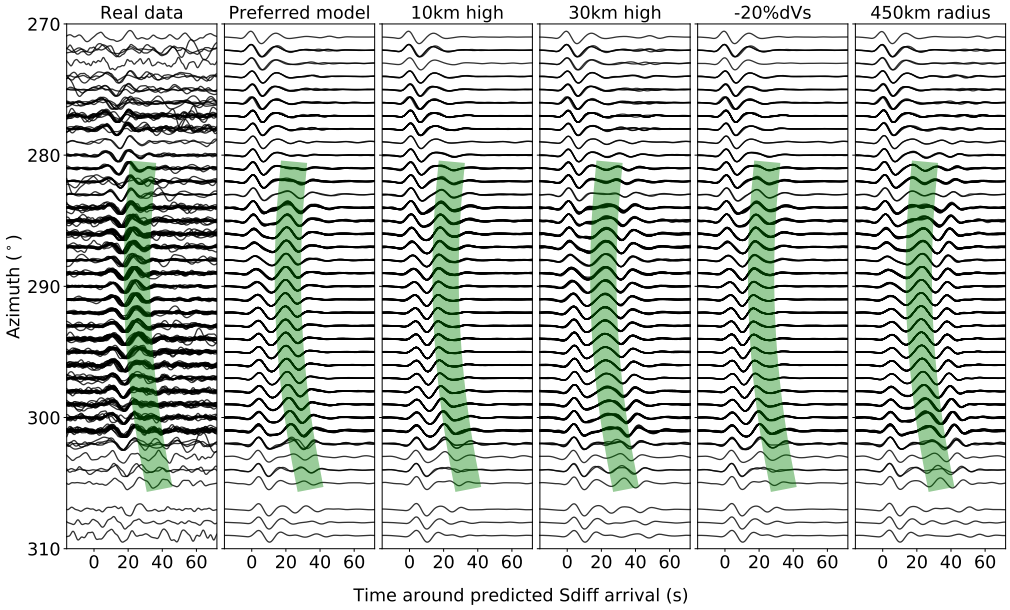

Figure S9. Waveform predictions for ULVZ models with different parameters for event A. Each model varies in only one parameter from our preferred model - height, V_S, or radius.

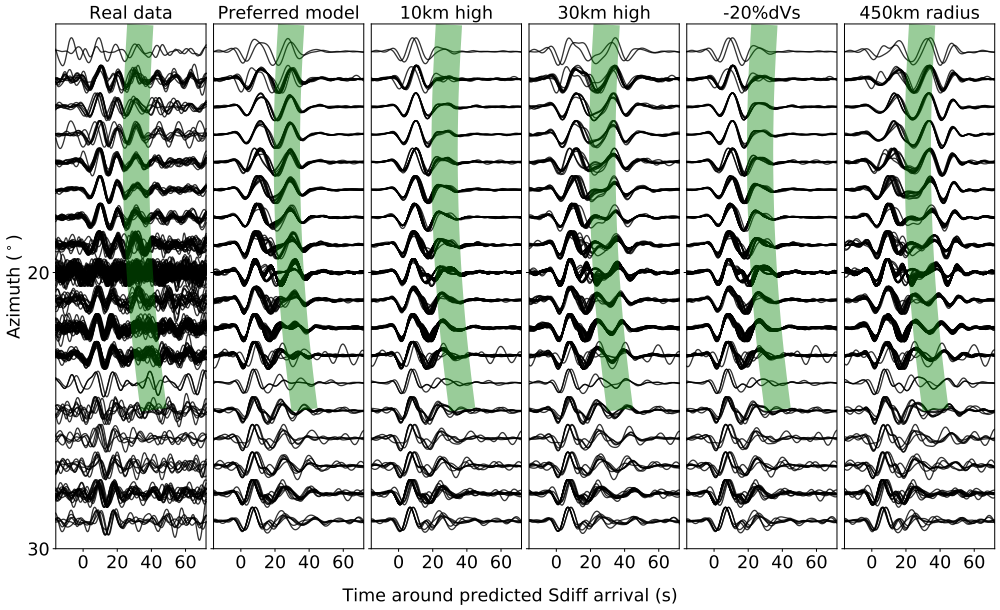

Figure S10. Waveform predictions for ULVZ models with different parameters for event C. Each model varies in only one parameter from our preferred model - height, V_S, or radius.

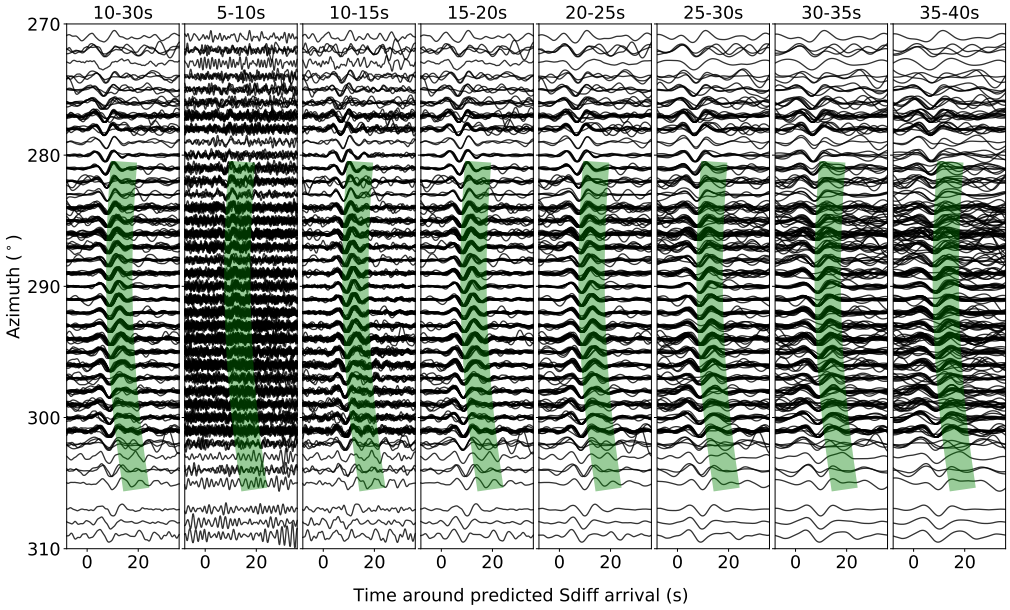

Figure S11. Waveform predictions for real data filtered to different narrow frequency bands for event A. The time frame where the postcursors are observed is highlighted across all plots.

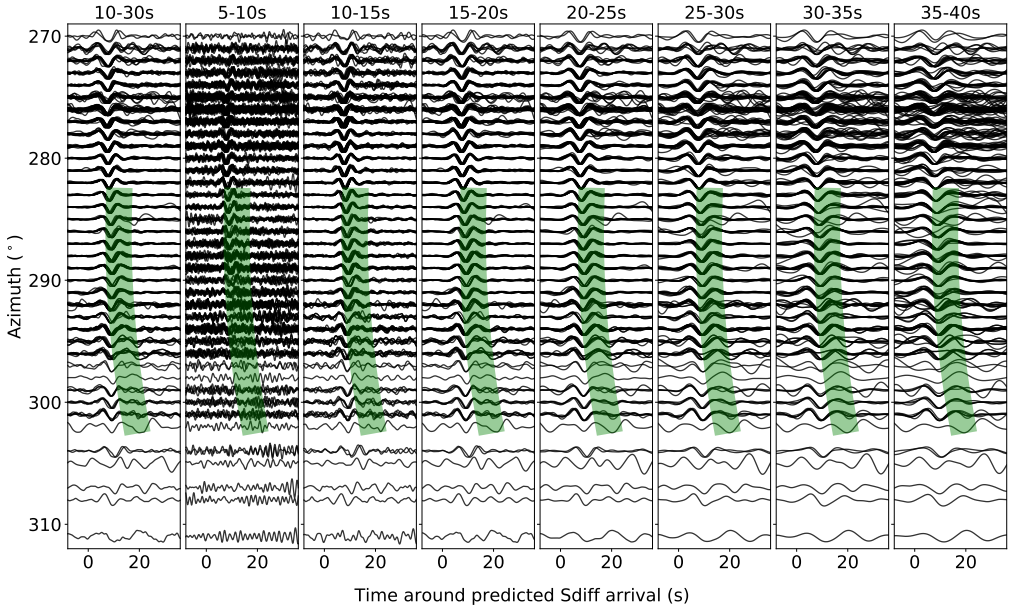

Figure S12. Waveform predictions for real data filtered to different narrow frequency bands for event B. The time frame where the postcursors are observed is highlighted across all plots.

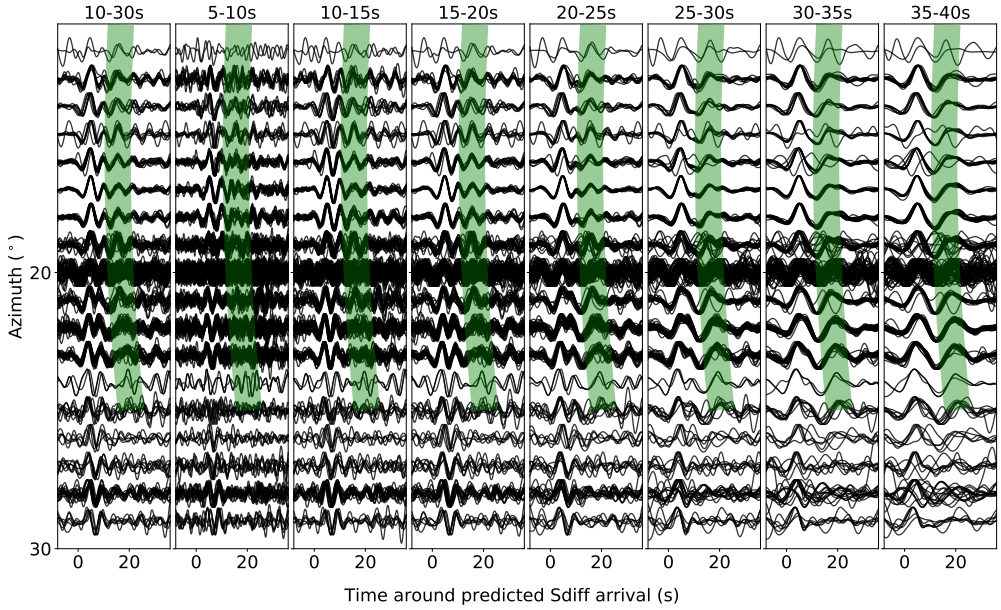

Figure S13. Waveform predictions for real data filtered to different narrow frequency bands for event C. The time frame where the postcursors are observed is highlighted across all plots.

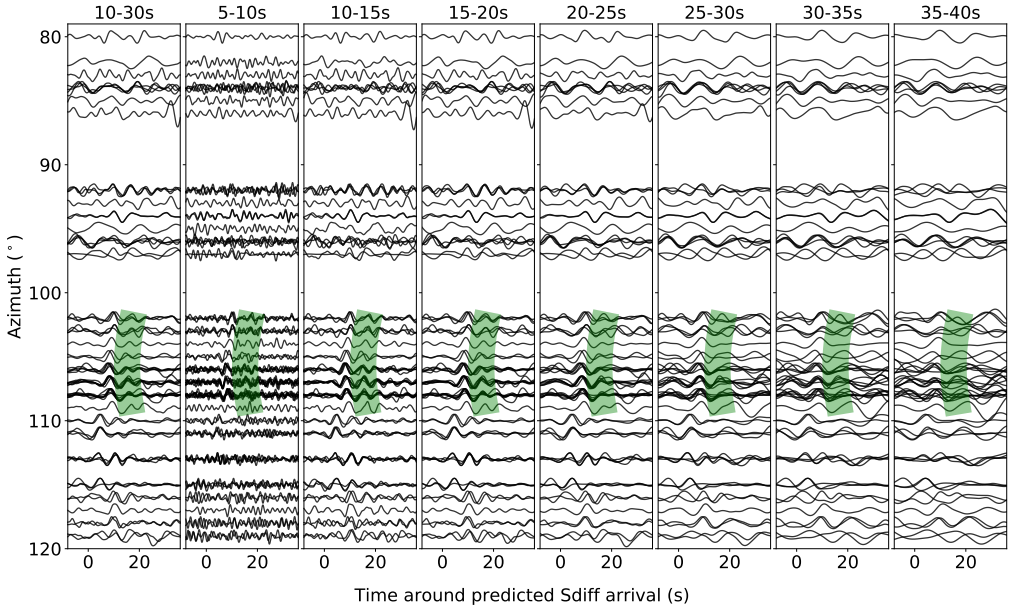

Figure S14. Waveform predictions for real data filtered to different narrow frequency bands for event D. The time frame where the postcursors are observed is highlighted across all plots.